

## Research Article

# Fracture Performance of a Large-Stone Asphalt Mixture Based on a Monotonic Tensile Overlay Test

Jianhui Wei <sup>1</sup>, Tao Fu <sup>2</sup>, and Junlin Liang <sup>2</sup>

<sup>1</sup>College of Architecture and Engineering, Shangqiu Normal University, 476000 Shangqiu, China

<sup>2</sup>College of Civil Engineering and Architecture, Guangxi University, 530004 Nanning, China

Correspondence should be addressed to Junlin Liang; [ljl\\_1217@126.com](mailto:ljl_1217@126.com)

Received 5 November 2020; Revised 15 March 2021; Accepted 25 March 2021; Published 9 April 2021

Academic Editor: Yi Zhang

Copyright © 2021 Jianhui Wei et al. This is an open access article distributed under the Creative Commons Attribution License, which permits unrestricted use, distribution, and reproduction in any medium, provided the original work is properly cited.

A large-stone asphalt mixture (LSAM) is usually used as the base course of asphalt pavement to prevent the generation of cracks. However, there are few studies on the fracture performance and crack resistance of LSAMs. Under the monotonic tensile loading mode, the overlay test (OT) was explored to investigate the influence of different test factors on the cracking resistance and fracture performance. The study results indicated that a change in temperature and aging results in a variation in fractal dimension, the fracture energy of crack growth is higher than that of crack initiation, and fracture energy is increased to a certain extent by decreased temperature, an increased loading rate or increased aging. Finally, a constitutive model is established based on the disturbed state concept (DSC), and the proposed constitutive model is consistent with the test results.

## 1. Introduction

Cracking is a common type of damage in pavement engineering [1, 2], especially for semirigid base layers. The cracking of asphalt pavement is affected not only by the thickness and stiffness of the pavement but also by the crack type and load position relative to the crack. To mitigate the generation of cracking and delay the propagation of cracks, technicians worldwide have carried out many studies and proposed measures to study the initiation and expansion of cracking. In recent decades, fracture mechanics has been used as a tool to study this phenomenon. In this framework, the cracking resistance of asphalt mixtures is determined using the fracture toughness or fracture energy, which can be determined using different testing methods, such as semi-circular bend (SCB) and edge notch disc bend (ENDB) [3–6]. The fracture toughness of asphalt mixture is significantly affected by temperature and air voids [7–9]. At low temperature, the viscoelastic behavior of asphalt mixtures changes to elastic behavior, which makes asphalt mixtures have higher stiffness at low temperature, thus improving the

fracture toughness, while increasing the temperature will weaken the chemical structure of bitumen. With the increase in air voids in asphalt mixtures, the corresponding fracture toughness value decreases [10–12], especially for asphalt mixtures with fine-grained siliceous aggregates. To some extent, the reduction of air voids reduces the number of bubbles as the stress concentration and correspondingly increases the fracture toughness of the material. Asphalt mixtures are multiphase composite materials, and their mechanical properties are also affected by the size and distribution of aggregates [13, 14]. Coarse aggregates can change the crack propagation path locally, which can improve the fracture resistance of materials under shear loading [15]. The crack propagation path is also affected by the elastic modulus difference of each component of the asphalt mixture. Due to the different modulus of aggregates and asphalt binder, the crack will propagate along the interface of aggregate asphalt binder [16]. From the micro-point of view, considering the material heterogeneity is helpful to study the cracking mechanism of asphalt mixtures [17, 18], the results showed that the pavement stress

concentration caused by the heterogeneity of asphalt mixture may be one of the main factors leading to pavement cracking [19]. It is a better solution to use modified asphalt mixtures to prevent pavement cracking. The research shows that the fracture toughness of modified asphalt mixtures has been greatly improved [20]. Pirmohammad used SCB tests to investigate the effects of different crack type on the fracture toughness of different modified hot mix asphalt mixtures, and the results showed that modified asphalt mixtures showed higher fracture toughness values than unmodified asphalt mixtures [21]. Mixtures containing crumb rubber (CR) and styrene butadiene styrene (SBS) have obvious effects on enhancing the fracture toughness of modified asphalt, and the fracture toughness of modified asphalt increases greatly than unmodified asphalt mixtures [22]. Pirmohammad et al. used SCB to investigate the effect of carbon nanotube modifier on the fracture resistance of asphalt mixtures [23]. The results showed that higher percentages of carbon nanotube can improve the fracture resistance of asphalt mixture under pure mode I. The application of carbon nanotubes can not only reduce the phase angle of asphalt binder but also improve the storage modulus of asphalt binder, which can enhance the performance of asphalt binder. In addition, increasing the loading rate can also improve the fracture resistance [9, 24–26]. With increasing loading rate, the elastic behavior of the asphalt mixture becomes more obvious. Generally, geosynthetic interlayers [27, 28] are also used to prevent the initiation and propagation of reflective cracking. Compared with ordinary asphalt concrete, large-stone asphalt mixtures (LSAMs) (which is an asphalt mixture with the largest nominal aggregate size greater than 26.5 mm that is used in pavement construction) have the characteristic of a large particle size, which can weaken the transmission of stress and strain and weaken the stress concentration, thus mitigating the initiation and propagation of cracking [13]. This may be because the coarse aggregate in the matrix asphalt mixture provides better stone-to-stone contact, which can cause higher internal friction, thus helping to form the skeleton structure and having a higher impact on the stiffness modulus [29]. Aggregates have a certain interference effect on crack propagation, can effectively reduce the configuration force at the crack tip, and significantly improve the crack resistance of asphalt mixtures. With increasing aggregate size, the inhibition effect of aggregates on crack growth also increases, which shows that the configuration force of the crack tip decreases gradually. With increasing aggregate size, the proportion of mode I cracks decreases [19].

However, at present, the main research on LSAMs is focused on the grading design method and the formation method [30]. Hao et al. proposed new laboratory methods and indexes to characterize segregation by studying the segregation phenomenon of LSAMs in the process of production and transportation and concluded that the Bailey method is more suitable for the LSAM grading design [31]. Based on the concept of stone-to-stone skeleton structures, Huang et al. investigated the applicability of the large-scale Marshall method and compaction method to specimen formation and determined the best ranges of asphalt content

(3.1%~3.6%), asphalt film thickness (13~16  $\mu\text{m}$ ), and air void (13%~18%), which showed that the LSPM has good water permeability, rutting resistance, and reflective crack resistance [32]. Mascarenhas et al. used LSAMs to repair two test road sections in Brazil and used the French wheel tracking test to study the linear viscoelastic properties of LSAMs. The results show that LSAMs have good rutting resistance [33].

The above literature shows that there are many studies of asphalt concrete at present. However, there are few studies on the fracture performance of LSAMs. Thus, a research method is proposed to investigate the fracture performance of LSAMs, and the constitutive equation in a monotonic tensile test is established based on the disturbed state concept (DSC).

## 2. Materials and Test Methodology

In this study, the specimen was composed of an LSAM-30 asphalt mixture. AH-70 matrix asphalt and limestone were used as the binder and aggregate, respectively. The target gradation of LSAM-30 is shown in Table 1. The LSAM-30 test results obtained by the Marshall test are shown in Table 2, with the technical specifications of LSAM-30. The optimum asphalt aggregate ratio was determined to be 3.38% by the Marshall test. In accordance with the requirements of the rutting plate, the LSAM specimens were trimmed to 150 mm  $\times$  100 mm  $\times$  60 mm from the rutting plate with dimensions of 300 mm  $\times$  300 mm  $\times$  100 mm. Before molding the rutting plate, the loose asphalt mixture was heated in an oven at 135°C  $\pm$  0.5°C for 4 hours  $\pm$  5 min. Then, the specimens were placed in an oven at 85°C  $\pm$  0.5°C for 3 days. Compared to the conventional aging method where the aging time is fixed at 5 days at 85°C, the aging time was reduced to 3 days in this study because the conventional aging time is equivalent to the aging conditions of asphalt pavement with a service life of 5–7 years, while early cracks of asphalt pavement appear in the first 2–3 years after completion. The results of asphalt and aggregate testing are given in Tables 3 and 4.

To propagate cracks in one direction, the temperature is usually set below 0°C. Stable crack propagation usually needs to be observed at a higher temperature, generally at approximately 25°C. In this experiment, the temperature conditions in Table 5 were selected according to the laboratory conditions and Guangxi climate characteristics. Another important parameter is the loading rate. Under the condition of a low loading rate, the asphalt mixture shows creep characteristics, while under the condition of a high loading rate, the fracture propagation characteristics of the asphalt mixture are not obvious. To obtain the stable crack propagation process, the influence of different loading rates on the OT test of LSAMs is studied in this paper.

Therefore, using the monotonic tensile OT test [34, 35], different test conditions for studying the fracture performance of LSAM were investigated in this study, including the loading rate, temperature, asphalt aggregate ratio, and aging. The specific test conditions are shown in Table 5. The experimental loading diagram, OT loading schematic diagram, and load-displacement curve under single tension

TABLE 1: Aggregate gradation for LSAM-30.

Size (mm)	37.5	31.5	26.5	19	16	13.2	9.5	4.75	2.36	1.18	0.6	0.3	0.15	0.075
Passing rate (%)	100	97.6	86.6	70.0	63.4	57.1	49.0	34.3	24.0	16.8	11.9	8.2	5.7	4.0

TABLE 2: Marshall test results and technical specifications for LSAM-30.

Asphalt aggregate ratio (%)	Volume of air voids, VV (%)	Voids filled with asphalt, VFA (%)	Voids in mineral aggregate, VMA (%)	Marshall stability (kN)	Flow value (0.1 mm)
3.38%	3.4	59.1	11.9	30	65
Technical specifications	3~6	60~75	>11	>15	40~70

TABLE 3: Properties of asphalt material.

Items	Units	Specification limits	Test results	Standard
Penetration (25°C, 5 s, 100 g)	0.1 mm	60~80	70.2	T 0604-2011
Ductility (15°C, 5 cm/min)	cm	≥100	150	T 0605-2011
Softening point	°C	≥46	47.1	T 0606-2011
Density (15°C)	g/cm <sup>3</sup>		1.028	T 0603-2011
RTFO at 163°C for 5 h				
Quality change (%)	%	±0.8	-0.2035	T 0609-2011
Residual penetration ratio (%)	%	≥61	70.5	T 0604-2011
Residual ductility (5°C)	cm	≥6	8.6	T 0606-2011

TABLE 4: Properties of aggregate.

Items	Units	Coarse aggregate		Fine aggregate	
		Limits	Test results	Limits	Test results
Crushed stone value	%	≤28.0	21.6	—	—
Los Angeles abrasion loss	%	≤30	18.4	—	—
Apparent relative density	g/cm <sup>3</sup>	≥2.50	2.75	≥2.50	2.746
Water absorption	%	≤3.0	0.79	—	—
Content (<0.075 mm)	%	≤1.0	0.2	—	—
Acicular content	%	≤15.0	3.2	—	—
Methylene blue value	g/kg			2.5	1.2

TABLE 5: The specific test conditions.

	Temperature	Asphalt aggregate ratio	Loading rate	Aging
Group 1	25°C	3.38%	1 mm/min, 2 mm/min, and 3 mm/min	Nonaging
Group 2	5°C, 15°C, 25°C, and 30°C	3.38%	3 mm/min	Nonaging
Group 3	25°C	3.38%, 3.6%, and 3.9%	3 mm/min	Nonaging
Group 4	25°C	3.38%	3 mm/min	Short aging and long aging

conditions are given in Figure 1. The displacement control mode is adopted in the test, and the test is terminated when the specimen is completely broken or the opening displacement is 20 mm. In the test, epoxy resin was used to paste the test pieces on the steel plates. The spacing between the steel plates was controlled by a 2 mm thick gasket. Transparent tape was pasted on the gasket to prevent the glue from sticking with the gasket, which was difficult to remove. Wood chips were used to evenly smear the glue on the steel plates, and the amount of glue was fully spread on the steel plates. After the specimen was pasted, the weight was placed on the specimen, and the weight and gasket were

removed after 12 h at room temperature. Before the test, the specimens were placed in an environmental box for heat preservation for at least 4 h.

### 3. Fracture Performance and Constitutive Model

*3.1. Expression of the Fracture Performance.* The primary output from a typical monotonic OT test is the load-displacement curve, as shown in Figure 1, which is used to calculate the fracture parameters of the test sample. Figure 1 shows that there are two different stages in crack

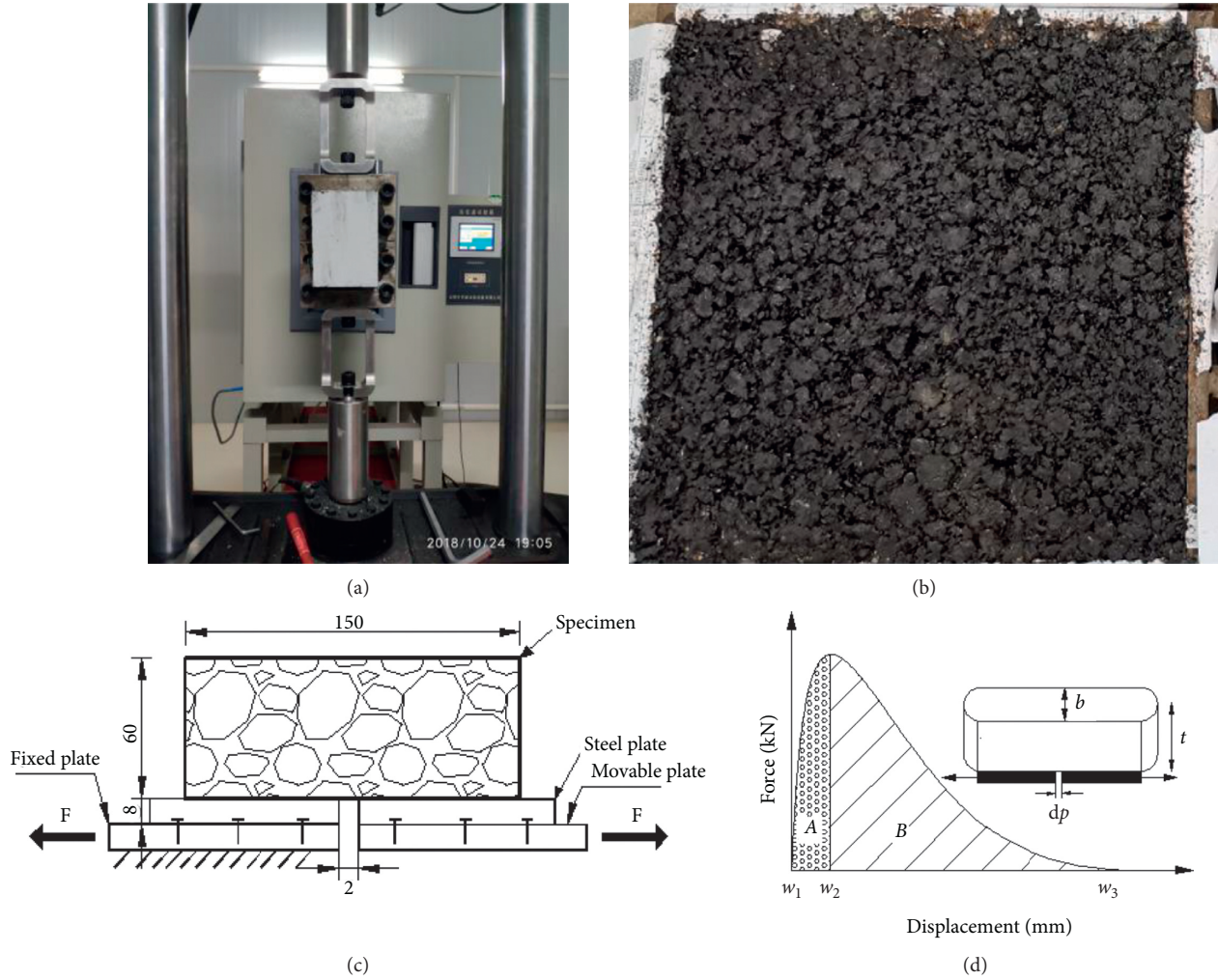


FIGURE 1: OT schematic diagram (mm), sample setup, and load vs. displacement during a typical monotonic OT test.

propagation: the crack initiation stage (area A) and the crack propagation stage (area B).

The total fracture energy is calculated by

$$G_f = \frac{1}{tb} \int f(w)dw, \quad (1)$$

where  $f(w)$  is the load-displacement curve function and  $t$  and  $b$  are the thickness and width of the specimen, respectively. The fracture energy at the crack initiation stage is calculated

$$G_A = \frac{1}{tb} \int_{w_1}^{w_2} f(w)dw. \quad (2)$$

The fracture energy during fracture propagation is calculated by

$$G_B = \frac{1}{tb} \int_{w_2}^{w_3} f(w)dw. \quad (3)$$

Therefore, the total fracture energy is calculated by

$$G_f = G_A + G_B = \frac{1}{tb} \int_{w_1}^{w_3} f(w)dw, \quad (4)$$

where  $w_1$ ,  $w_2$ , and  $w_3$  are different displacement corresponding to load-displacement curve, respectively.

**3.2. Disturbed State Concept (DSC).** DSC [36, 37] is a unified method to describe the deformation of materials from the initial state to a new equilibrium state or a failure state under the action of external factors. It is used to investigate the constitutive model of engineering materials. In DSC, materials are considered to be a mixture of two interacting materials in the relatively intact state (RI) and fully adjusted state (FA). It is considered that external loading disturbs the material structure and changes the internal microstructure of the material. The disturbance  $D$  is generally defined by the relationship of the observed state, RI, and FA, and the behavior of materials in any specific state can be expressed by the disturbance  $D$  using the response of two basic states' (RI and FA) equations (5). Figure 2 shows a schematic diagram of the mechanical response of a material in a DSC model:

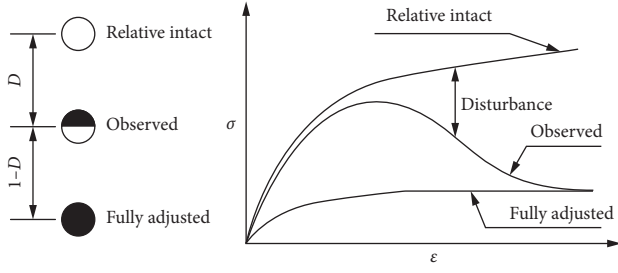


FIGURE 2: Schematic of stress vs. strain behavior in DSC.

$$d\sigma_{ij}^a = (1 - D)d\sigma_{ij}^i + D d\sigma_{ij}^c + D d(\sigma_{ij}^c - \sigma_{ij}^i), \quad (5a)$$

$$d\sigma_{ij}^a = (1 - D)C_{ijkl}^i d\epsilon_{kl}^i + DC_{ijkl}^c d\epsilon_{kl}^c + D d(\sigma_{ij}^c - \sigma_{ij}^i), \quad (5b)$$

where  $\sigma_{ij}$  and  $\epsilon_{kl}$  are stress and strain, respectively,  $C_{ijkl}$  is the elastic coefficient, and superscript  $a$ ,  $i$ , and  $c$  represent the observation state, RI, and FA, respectively.

The RI generally represents the initial structural state of the material, excluding the factors of microcracks and damage. Generally, it is defined by theoretical models, such as the linear elastic model, the elastic-plastic model, or the viscoelastic plastic model. It is assumed that RI is a linear elastic model. Finally, for homogeneous and isotropic materials, the elastic coefficient tensor is  $\sigma_{ijkl}^i = E_0$  in the uniaxial stress state, where  $E_0$  is the elasticity modulus.

$$\sigma_{ij}^i = E_0 \epsilon_{ij}^i, \quad (6)$$

where  $\sigma_{ij}^i$  and  $\epsilon_{ij}^i$  are the stress and the strain in RI, respectively.

The FA, which is defined based on the approximation of the ultimate asymptotic response of the material, cannot be observed and measured in the laboratory Figure 2. Materials in FA are similar to bubbles in solid materials, which are randomly distributed. This part of the material can bear a load. Only after the final adjustment is the material completely damaged and will not bear a load. The FA is defined as the critical tensile stress when the material breaks in uniaxial tension in this study.

The disturbance  $D$  represents the coupling mechanism between the RI and FA states and is defined by deviations in observed behaviors and from the RI or FA state. In a monotonic tensile test, the secant slope of each point of the load-displacement curve to the origin decreases with the increase in tensile displacement. Therefore, the disturbance  $D$  is defined by

$$D = \frac{E^i - E^a}{E^i - E^c}, \quad (7)$$

where  $E$  is the secant slope of each point of the load displacement curve to the origin. The relationship between the disturbance  $D$  and the nominal strain is established by

$$D = D_u (1 - \exp(-A\epsilon^Z)), \quad (8)$$

where  $\epsilon = (D_{\max}/d_0)$  is the nominal tensile strain,  $D_{\max}$  is the displacement measured in the test, and  $d_0$  is the gap between the base plates,  $A$ ,  $Z$ , and  $D_u$  are fitting parameters, and  $\exp$  is a power function. Therefore, the disturbance constitutive model of LSAM is expressed by

$$d\sigma_{ij}^a = (1 - D)E d\epsilon_{ij}^i + dD(\sigma_{ij}^c - E\sigma_{ij}^i). \quad (9)$$

## 4. Results and Discussion

### 4.1. Influence of Different Factors on the Fracture Performance.

The load-displacement curves and the test results are shown in Figure 3 and Table 6, respectively, under different test conditions. Both Figure 3 and Table 6 show that the enclosed area in the load-displacement curve in the crack propagation stage is larger than the enclosed area in the crack initiation stage, indicating that the energy for crack initiation is less than that for crack propagation.

In Figure 3(a), it can be seen that there was no significant difference between the mechanical properties and load-displacement curves obtained from the loading rates of 3 (mm/min) and 4 (mm/min). However, the mechanical properties and load-displacement curves obtained from the loading rate of 5 (mm/min) were significantly higher than those of 3 (mm/min) and 4 (mm/min). This result indicates that different loading rates have an influence on the fracture performance. By and large, the test results are consistent with the law that the strength increases with the increase of the loading rate. The possible reason is that the uneven distribution of coarse aggregates in LSAMs results in deviations in the test results. The coarse aggregates change the crack propagation path in the vertical direction, resulting in inclined cracks from the bottom to the loading end. This changes the stress state of the specimen and further increases the probability of the specimen separating from the contact surface of the bottom and the fixture. The bending stress in the specimen increases, which changes the stress state of the specimen. The loading end needs to share part of the load to overcome the bending stress, which makes the measured peak load increase.

As shown in Table 6, the total fracture energy  $G_f$ , the fracture energy in crack propagation  $G_B$ , and the peak load generally show an increasing trend with the increase in the loading rate. The fracture energy of crack initiation measured at the higher loading rate is also higher. Therefore, to reduce the influence of the loading rate, a loading rate of 3 (mm/min) is adopted in the subsequent tests in this study.

As shown in Figure 3(b), there is no significant effect on the load-displacement curve by changing the asphalt aggregate ratio. The three load-displacement curves basically coincide before the peak point, and the influence of the asphalt aggregate ratio on the peak load is not obvious. The

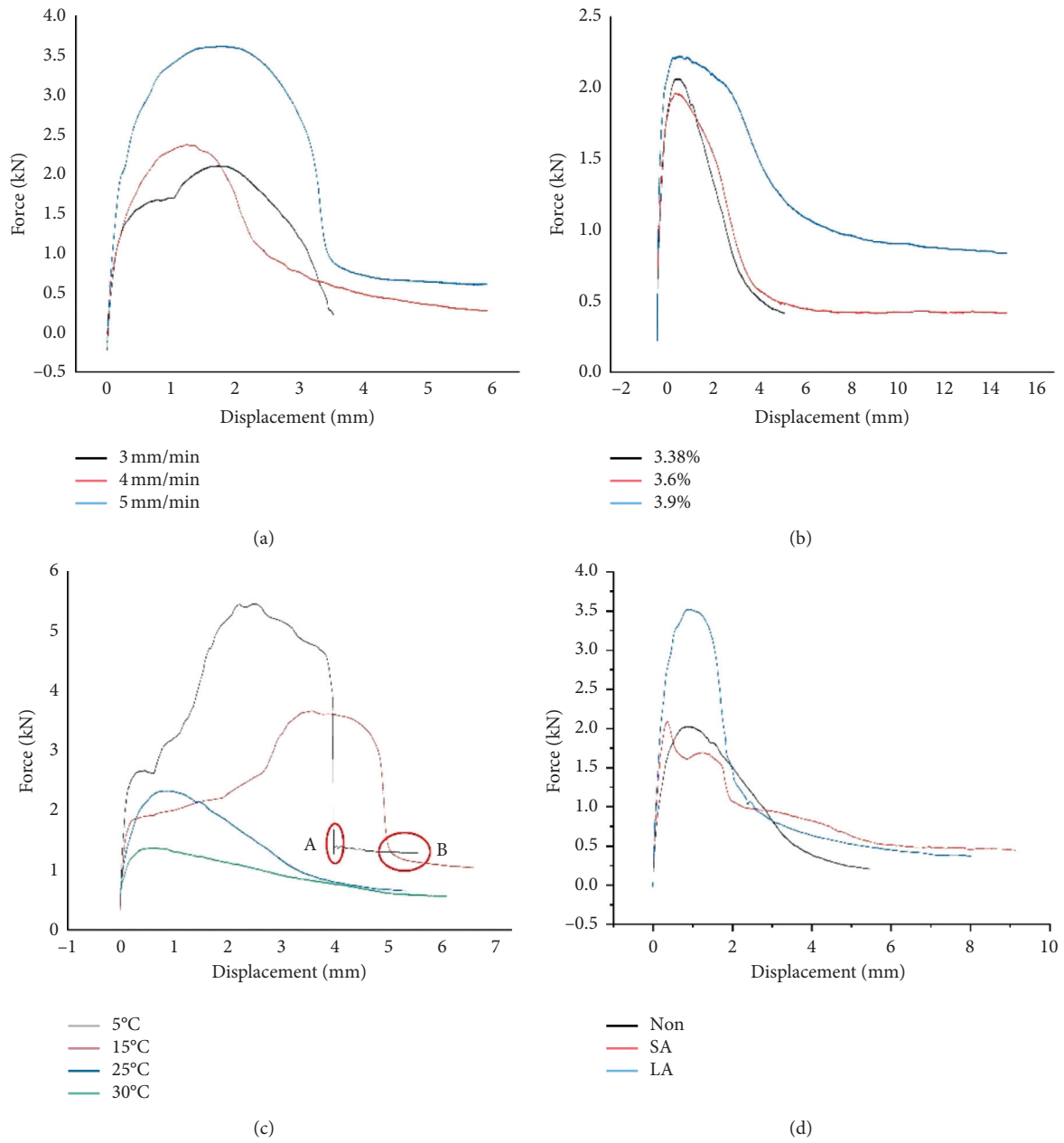


FIGURE 3: Load-displacement curves of LSAM with monotonic OT corresponding to the (a) loading rate, (b) asphalt aggregate ratio, (c) temperature, and (d) degree of aging.

TABLE 6: Test results of LSAM.

	Standard	4 mm/min	5 mm/min	3.6%	3.9%	5°C	15°C	30°C	SA	LA
$N$ (kN)	1.907	2.434	3.228	1.834	2.085	4.603	3.731	0.933	2.771	3.281
$G_A$ (J/m <sup>2</sup> )	374.579	462.171	972.597	195.274	318.373	1605.106	1603.09	77.337	282.17	396.862
$G_B$ (J/m <sup>2</sup> )	802.282	717.962	1111.641	633.48	800.072	1971.753	1540.593	606.976	759.138	1184.7
$G_f$ (J/m <sup>2</sup> )	1176.861	1180.133	2084.238	828.921	1118.445	3576.859	3143.683	684.313	1041.309	1448.502

Note. The standard in Table 6 indicates that the test conditions are as follows: loading rate of 3 mm/min, asphalt aggregate ratio of 3.38%, temperature of 25°C, and nonaging.

mechanical properties of the asphalt aggregate ratio of 3.6% are worse for the three different asphalt aggregate ratios.

As shown in Figure 3(c) and Table 6, the peak load and fracture energy  $G_A$ ,  $G_B$ , and  $G_f$  decrease with increasing temperature. In the higher temperature environment (25°C and 30°C), the LSAM has certain ductility characteristics, and the load-displacement curves are relatively smooth and have a relatively large displacement. As the temperature increases, the peak load decreases, as does the tensile strength. In contrast, the slope of the load-displacement curve increases with the decrease in temperature in crack propagation. In a lower temperature environment (5°C and 15°C), the load will gradually increase with the increase in displacement until specimen fracture, after which the load will decrease. Instantaneous fractures in point A and B in Figure 3(c) will occur as the temperature drops to 5°C, which indicates that the brittle behavior of LSAM is obvious in a low-temperature environment, the propagation rate of cracking is faster, and the propagation stage is short. This is also a common feature of asphalt mixtures.

By and large, the test is consistent with the law that the tensile displacement of the asphalt mixture decreases with decreasing temperature. In the high-temperature environment, the main crack propagation needs to bypass the coarse aggregate, which changes the aggregate propagation path and makes the crack deviate from the vertical path. The results show that there is an obvious crack propagation stage, the tensile displacement increases continuously after the peak load, and the load-displacement curve shows an obvious softening stage. In a low-temperature environment, asphalt mixtures show brittleness, decreasing in ductility and in tensile displacement. There is no obvious softening stage in the load-displacement curve. In addition, sliding failure also occurs on the contact surface between the specimen and the fixture, which is also the reason for the increase in displacement.

Figure 3(d) indicates that the load-displacement curve for long-term aging at 3 days is significantly higher than that for short-term aging and nonaging. The slope of the descending section of the load displacement curve increases with increasing aging, which indicates that the cracking rate is faster after aging. As shown in Table 6, the peak load increases gradually as aging increases, and the crack propagation fracture energy ( $G_B$ ) and the total fracture energy ( $G_f$ ) have an increasing trend with the increase in the degree of aging.

The decrease in temperature and the increase in the loading rate and degree of aging have obvious effects on the mechanical behavior of the test, which makes the material behavior change from viscoelastic behavior to elastic behavior. The peak load of the test is increased, but the tensile displacement is not significantly reduced. This makes the fracture energy increase to a certain extent. This is related to the size of the specimen and the size of the aggregate. Since the coarse aggregate changes the crack propagation path, obvious large deformation characteristics can be observed on the whole side of the specimen. In addition, the cracks will also expand along the horizontal direction, which makes the measured displacement increase. The longer the crack

propagation path is, the longer the time it takes for the crack to gradually expand from the bottom of LSAM to the asphalt pavement surface under the same load and the more the energy is required for propagation of reflection cracks, which can delay the crack propagation. In addition, some slip deformation can be observed at the interface between the specimen and the fixture, which also increases the displacement. These two aspects indicate that the LSAM has a positive effect on inhibiting fracture propagation.

*4.2. Fractal Characteristics of Fractures.* Asphalt mixtures are a type of composite material with complex geometric characteristics, and the internal microporous structure has fractal characteristics after fracture. In this study, the box dimension is used to describe the fractal characteristics of the fracture surface. After obtaining the original picture of the fracture surface Figure 4, Photoshop CS6 and MATLAB R2017a are used to process the original picture and obtain the high definition area as the calculation area. Next, the original image is converted to a grayscale image. The Otsu algorithm [38] is used to segment the image to obtain a binary image of the cracks, as shown in Figure 4. Using different mesh sizes  $\varepsilon$  to segment the binary image, MATLAB R2017a is employed to obtain the mesh number  $N$  of covering cracks corresponding to different mesh sizes. The sequence  $(\log(1/\varepsilon), \log N)$  is plotted in double logarithmic coordinates, and the fracture is considered to have a fractal characteristic if there is a good linear correlation between  $\log(1/\varepsilon)$  and  $\log N$ . An example of the original fracture photograph and the binary image of the asphalt aggregate ratio of 3.6% are shown in Figure 4, while Table 7 shows the box dimension calculation results. As shown in Figure 4,  $\log(1/\varepsilon)$  and  $\log N$  have a good linear relationship, with a correlation coefficient greater than 95%. This indicates that the fracture surface of LSAM has an obvious fractal characteristic and that fractal theory is suitable to investigate the fracture performance of LSAM.

The fracture energy represents the energy for crack growth per unit area. The calculation of the fracture energy is inseparable from the fracture surface area such that the higher the fractal dimension is, the more complex the fracture geometry path is and the higher the fracture energy is. Table 7 shows the calculation results of the fractal dimension under different conditions. It can be seen from the previous discussion that the brittleness of LSAM is obvious in the low-temperature environment, and after aging, the fracture load is higher, the fracture energy is larger, the fracture surface is more zigzag and complex, and the fractal dimension is larger.

*4.3. Disturbed Constitutive Model.* Figure 5 shows the stress-strain relationship under different test conditions, which indicates that the theoretical calculation results are consistent with the test results and that the model proposed in this study can basically reflect the mechanical response of LSAM under uniaxial tensile tests. The theoretical calculation results are very close to the test results before the peak load, but the load-displacement curve

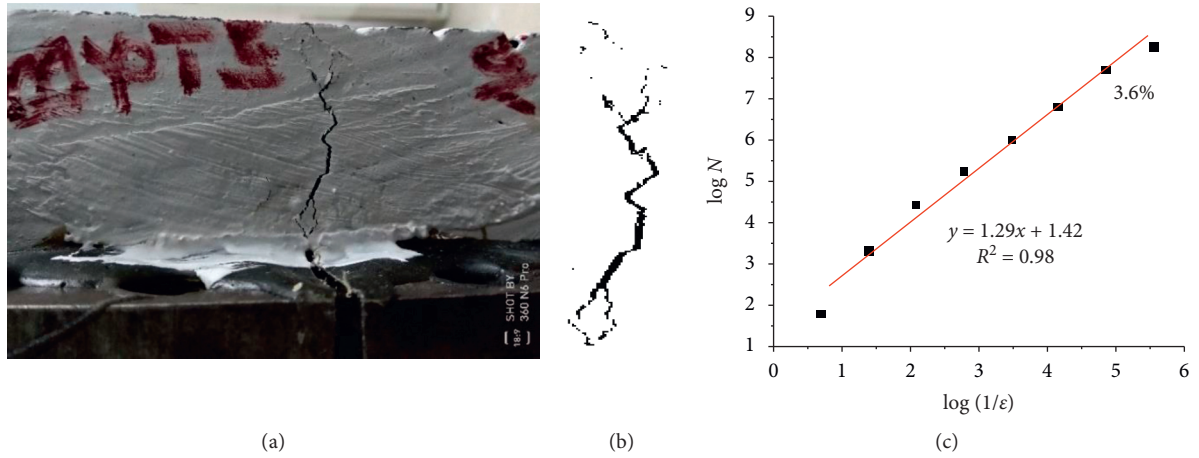


FIGURE 4: Fracture diagram of specimens and a binary image of a LSAM specimen (asphalt aggregate ratio = 3.6%).

TABLE 7: Test results of fractal dimensions for LSAM.

	5°C	15°C	25°C	30°C	SA	LA	3.6%	3.9%
Fractal	1.496	1.443	1.418	1.403	1.455	1.531	1.261	1.333

Note: the test results in the 25°C column in the table are under the conditions of nonaging and an asphalt aggregate ratio of 3.38%.

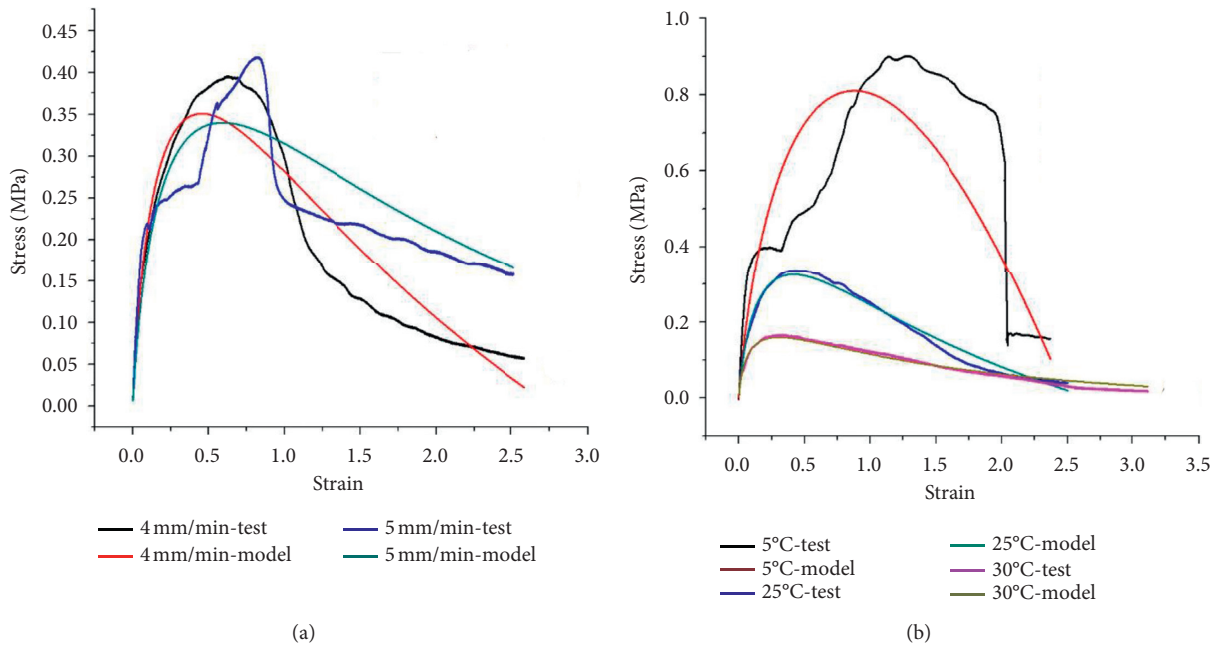


FIGURE 5: Continued.

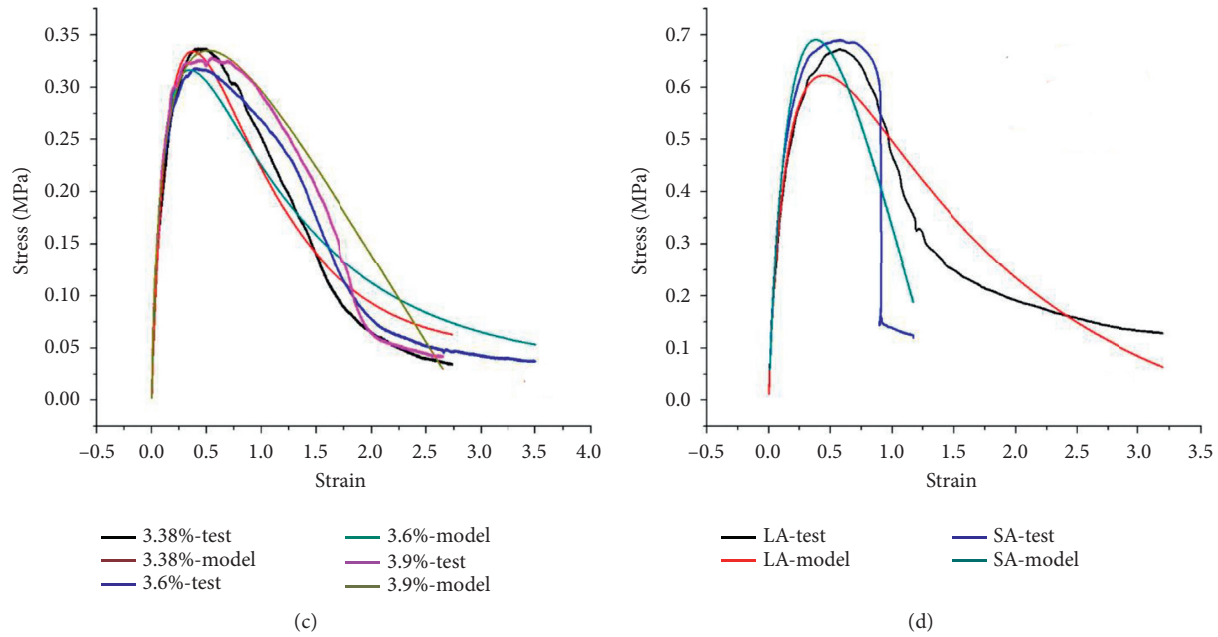


FIGURE 5: Comparisons between the test and model corresponding to the (a) loading rate, (b) temperature, (c) asphalt aggregate ratio, and (d) degree of aging.

calculated by the model in the softening stage deviates from the test results after the peak load. The deviation between the experimental and theoretical models has both the problems of the model and the reasons for the test itself. Due to the characteristics of LSAM (such as heterogeneous materials), the determination of the critical value has a greater discreteness and randomness, which inevitably leads to a deviation between the theoretical calculation results and test results. Therefore, it is necessary to further study the mechanical response of LSAMs.

During the single tension test at 5°C, the specimens show obvious brittle behavior. With the increase in tensile displacement, the load increases gradually until the load reaches the peak; then, the specimen suddenly breaks. And, there is no obvious crack propagation process and softening stage in the load-displacement curve, but the constitutive model is a continuous equation, which can reflect the softening phenomenon of loading. This leads to the obvious difference between the measured curve and the calculated curve in the softening stage.

## 5. Conclusions

An OT with a monotonic tensile test was carried out under different loading rates, different temperatures, different asphalt aggregate ratios, and aging. A constitutive model was established based on the disturbed state concept. The conclusions are as follows:

- (1) The fractal dimension can be used as an evaluation index for the fracture performance such that the higher the fractal dimension is, the higher the

fracture energy is. Decreasing temperature and aging result in a slight variation in fractal dimension.

- (2) The fracture energy of crack propagation is higher than that of crack initiation. The total fracture energy ( $G_f$ ), the crack propagation fracture energy ( $G_B$ ), and the peak load increase with the increase in the loading rate; the fracture energy parameters ( $G_A$ ,  $G_B$ , and  $G_f$ ) decrease with the increasing in temperature; the fracture energy of crack propagation ( $G_B$ ) and the total fracture energy ( $G_f$ ) increase with the increasing in aging.
- (3) Aging and low temperature can improve the tensile strength to a certain extent but weaken crack propagation, which indicates that aging and cooling can accelerate the crack growth rate. LSAM more easily cracks before reaching the tensile strength in a low-temperature environment, but it can still be loaded continuously until the tensile strength is reached.
- (4) The constitutive model of LSAM is established based on DSC. The calculation results are consistent with the test results, which can be used to predict the mechanical response under a uniaxial tensile test.

## Abbreviations

- $G_A$ ,  $G_B$ , and  $G_f$ : The fracture energy corresponding to area A, area B, and area A + B in force-displacement curve
- $f(w)$ : The load-displacement curve function
- $t$  and  $b$ : The thickness and width of the specimen, respectively

$\omega_1, \omega_2,$ and $\omega_3$ :	The different displacement in load-displacement curve
$\sigma_{ij}, \epsilon_{kl},$ and $C_{ijkl}$ :	The stress tensor, strain tensor, and elastic coefficient
$E_0$ :	Elasticity modulus
$D_{\max}$ and $d_0$ :	The displacement measured in the test and the gap between the base plates
$A, Z,$ and $D_u$ :	Fitting parameters
exp:	A power function
$\epsilon$ :	The nominal tensile strain
LA:	The long aging
SA:	The short aging
Non:	Nonaging.

## Data Availability

The data used to support the findings of this study are available from the corresponding author upon request.

## Conflicts of Interest

The authors declare that they have no conflicts of interest.

## Acknowledgments

This study was based upon the work supported by the National Natural Science Foundation of China (Grant nos. 51168005 and 51268003).

## References

- [1] B. Golestani, B. Nam, M. Noori, J. An, and O. Tatari, "An optimum selection strategy of reflective cracking mitigation methods for an asphalt concrete overlay over flexible pavements," *International Journal of Pavement Engineering*, vol. 19, no. 1, pp. 48–61, 2018.
- [2] I. Gonzalez-Torre, M. A. Calzada-Perez, A. Vega-Zamanillo, and D. Castro-Fresno, "Evaluation of reflective cracking in pavements using a new procedure that combine loads with different frequencies," *Construction and Building Materials*, vol. 75, pp. 368–374, 2015.
- [3] A. Bahmani, M. R. M. Aliha, M. Jebalbarez Sarbijan, and S. S. Mousavi, "An extended edge-notched disc bend (ENDB) specimen for mixed-mode I+II fracture assessments," *International Journal of Solids and Structures*, vol. 193–194, pp. 239–250, 2020.
- [4] J. Bidadi, J. Akbaridoost, and M. R. M. Aliha, "Thickness effect on the mode III fracture resistance and fracture path of rock using ENDB specimens," *Fatigue & Fracture of Engineering Materials & Structures*, vol. 43, no. 2, pp. 277–291, 2020.
- [5] D. X. Lu, H. H. Bui, and M. Saleh, "Effects of specimen size and loading conditions on the fracture behaviour of asphalt concretes in the SCB test," *Engineering Fracture Mechanics*, vol. 242, p. 107452, 2021.
- [6] X. Wang, J. Zhang, K. Li, Y. Ding, and L. Geng, "Cracking analysis of asphalt mixture using semi-circle bending method," *Iranian Journal of Science and Technology, Transactions of Civil Engineering*, vol. 45, no. 1, pp. 269–279, 2021.
- [7] X. Li, M. O. Marasteanu, A. Kvasnak, J. Bausano, R. C. Williams, and B. Worel, "Factors study in low-temperature fracture resistance of asphalt concrete," *Journal of Materials in Civil Engineering*, vol. 22, no. 2, pp. 145–152, 2010.
- [8] D. X. Lu, M. Saleh, and N. H. T. Nguyen, "Evaluation of fracture and fatigue cracking characterization ability of nonstandardized semicircular-bending test for asphalt concrete," *Journal of Materials in Civil Engineering*, vol. 32, no. 8, 2020.
- [9] N. Shahryari, M. R. Keymanesh, and M. R. M. Aliha, "Specimen type effect on measured low-temperature fracture toughness of asphalt concrete," *Fatigue & Fracture of Engineering Materials & Structures*, vol. 44, no. 2, pp. 551–567, 2021.
- [10] M. R. M. Aliha and H. R. Fattahi Amirdehi, "Fracture toughness prediction using Weibull statistical method for asphalt mixtures containing different air void contents," *Fatigue & Fracture of Engineering Materials & Structures*, vol. 40, no. 1, pp. 55–68, 2017.
- [11] S. Pirmohammad and M. R. Ayatollahi, "Asphalt concrete resistance against fracture at low temperatures under different modes of loading," *Cold Regions Science and Technology*, vol. 110, pp. 149–159, 2015.
- [12] J. Ren and L. Sun, "Characterizing air void effect on fracture of asphalt concrete at low-temperature using discrete element method," *Engineering Fracture Mechanics*, vol. 170, pp. 23–43, 2017.
- [13] W. Liu, Y. Gao, and X. Huang, "Effects of aggregate size and specimen scale on asphalt mixture cracking using a micro-mechanical simulation approach," *Journal of Wuhan University of Technology-Material Science Edition*, vol. 32, no. 6, pp. 1503–1510, 2017.
- [14] H. Wang, J. Wang, and J. Chen, "Fracture simulation of asphalt concrete with randomly generated aggregate micro-structure," *Road Materials and Pavement Design*, vol. 19, no. 7, pp. 1674–1691, 2018.
- [15] C. Du, Y. Sun, J. Chen, H. Gong, X. Wei, and Z. Zhang, "Analysis of cohesive and adhesive damage initiations of asphalt pavement using a microstructure-based finite element model," *Construction and Building Materials*, vol. 261, p. 119973, 2020.
- [16] W. Xu, X. Wei, J. Wei, and Z. Chen, "Experimental evaluation of the influence of aggregate strength on the flexural cracking behavior of epoxy asphalt mixtures," *Materials*, vol. 13, no. 8, p. 1876, 2020.
- [17] Z. Fan, C. Du, P. Liu, D. Wang, and M. Oeser, "Study on interfacial debonding between bitumen and aggregate based on micromechanical damage model," *International Journal of Pavement Engineering*, pp. 1–9, 2020.
- [18] Y. Sun, C. Du, H. Gong, Y. Li, and J. Chen, "Effect of temperature field on damage initiation in asphalt pavement: a microstructure-based multiscale finite element method," *Mechanics of Materials*, vol. 144, p. 103367, 2020.
- [19] J. Du, C. Ai, S. An, D. Ren, and Y. Qiu, "Influence of aggregate interference on the crack propagation of asphalt concrete by the configurational force fracture criterion," *Construction and Building Materials*, vol. 265, p. 120293, 2020.
- [20] G. Shafabakhsh, M. Sadeghnejad, and R. Ebrahimnia, "Fracture resistance of asphalt mixtures under mixed-mode I/II loading at low-temperature: without and with nano SiO<sub>2</sub>," *Construction and Building Materials*, vol. 266, p. 120954, 2021.
- [21] S. Pirmohammad and H. Shabani, "Mixed mode I/II fracture strength of modified HMA concretes subjected to different temperature conditions," *Journal of Testing and Evaluation*, vol. 47, no. 5, pp. 20180848–20183371, 2019.
- [22] X. Xin, Z. Yao, J. Shi et al., "Rheological properties, micro-structure and aging resistance of asphalt modified with CNTs/

- PE composites,” *Construction and Building Materials*, vol. 262, p. 120100, 2020.
- [23] S. Pirmohammad, Y. Majd-Shokorlou, and B. Amani, “Experimental investigation of fracture properties of asphalt mixtures modified with Nano  $\text{Fe}_2\text{O}_3$  and carbon nanotubes,” *Road Materials and Pavement Design*, vol. 21, no. 8, pp. 2321–2343, 2020.
- [24] B. Doll, H. Ozer, J. J. Rivera-Perez, I. L. Al-Qadi, and J. Lambros, “Investigation of viscoelastic fracture fields in asphalt mixtures using digital image correlation,” *International Journal of Fracture*, vol. 205, no. 1, pp. 37–56, 2017.
- [25] J. Jiang, Q. Dong, F. Ni, and Y. Zhao, “Effects of loading rate and temperature on cracking resistance characteristics of asphalt mixtures using nonnotched semicircular bending tests,” *Journal of Testing and Evaluation*, vol. 47, no. 4, pp. 20170711–20172663, 2019.
- [26] H. Saeidi and I. Aghayan, “Investigating the effects of aging and loading rate on low-temperature cracking resistance of core-based asphalt samples using semi-circular bending test,” *Construction and Building Materials*, vol. 126, pp. 682–690, 2016.
- [27] V. V. Kumar and S. Saride, “Evaluation of cracking resistance potential of geosynthetic reinforced asphalt overlays using direct tensile strength test,” *Construction and Building Materials*, vol. 162, pp. 37–47, 2018.
- [28] S. Saride and V. V. Kumar, “Influence of geosynthetic-interlayers on the performance of asphalt overlays on pre-cracked pavements,” *Geotextiles and Geomembranes*, vol. 45, no. 3, pp. 184–196, 2017.
- [29] L. Garcia-Gil, R. Miró, and F. Pérez-Jiménez, “Evaluating the role of aggregate gradation on cracking performance of asphalt concrete for thin overlays,” *Applied Sciences*, vol. 9, no. 4, p. 628, 2019.
- [30] G. Yuan, P. Hao, D. Li, J. Pan, and S. Dong, “Optimization design and verification of large stone porous asphalt mixes gradation using compressible packing model,” *Construction and Building Materials*, vol. 230, p. 116903, 2020.
- [31] X. Feng, S. Ye, and P. Hao, “A new laboratory method to characterize gradation segregation of large stone asphalt mixtures,” *Construction and Building Materials*, vol. 38, pp. 1199–1203, 2013.
- [32] Y. Zhao and X. Huang, “Design method and performance for large stone porous asphalt mixtures,” *Journal of Wuhan University of Technology-Material Science Edition*, vol. 25, no. 5, pp. 871–876, 2010.
- [33] Z. M. G. Mascarenhas, M. S. Gaspar, K. L. Vasconcelos, L. L. B. Bernucci, and A. Bhasin, “Case study of a composite layer with large-stone asphalt mixture for heavy-traffic highways,” *Journal of Transportation Engineering, Part B: Pavements*, vol. 146, no. 1, p. 04019040, 2020.
- [34] V. M. Garcia and A. Miramontes, “Understanding sources of variability of overlay test procedure,” *Transportation Research Record*, vol. 2507, pp. 10–18, 2015.
- [35] V. M. Garcia, A. Miramontes, J. Garibay, I. Abdallah, and S. Nazarian, “Assessing crack susceptibility of asphalt concrete mixtures with overlay tester,” *Journal of Testing and Evaluation*, vol. 46, no. 3, pp. 20170006–20170933, 2018.
- [36] C. S. Desai, “Constitutive modeling of materials and contacts using the disturbed state concept: part 1-background and analysis,” *Computers & Structures*, vol. 146, pp. 214–233, 2015.
- [37] C. S. Desai, “Constitutive modeling of materials and contacts using the disturbed state concept: part 2-validations at specimen and boundary value problem levels,” *Computers & Structures*, vol. 146, pp. 234–251, 2015.
- [38] Y. Wang, J. Y. Zhang, J. X. Liu et al., “Research on crack detection algorithm of the concrete bridge based on image processing,” in *Proceedings of the 9th International Conference of Information and Communication Technology [ICICT-2019]*, S. Patnaik, Ed., pp. 610–616, Nanning, China, January 2019.